

Weierstraß-Institut für Angewandte Analysis und Stochastik

im Forschungsverbund Berlin e.V.

Preprint

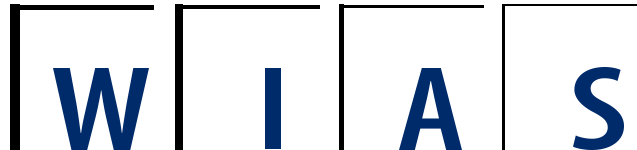
ISSN 0946 – 8633

Analysis of nonlocal neural fields for both general and gamma-distributed connectivities

A.Hutt¹ , Fatihcan M. Atay²

¹ E-Mail: hutt@wias-berlin.de ² E-Mail: atay@member.ams.org

No. 969
Berlin 2004



2000 *Mathematics Subject Classification.* 45J05 92C20.

Key words and phrases. nonlocal neural activity, space-dependent delay, stability analysis.

A.Hutt is supported by DFG Research Center Mathematics for key technologies: Modelling, simulation and optimization of real-world processes in Berlin / Germany.

Edited by
Weierstraß-Institut für Angewandte Analysis und Stochastik (WIAS)
Mohrenstraße 39
10117 Berlin
Germany

Fax: + 49 30 2044975
E-Mail: preprint@wias-berlin.de
World Wide Web: <http://www.wias-berlin.de/>

Abstract

This work studies the stability of spatially extended neuronal ensembles. We first derive the model equation from statistical properties of the neuron population. The obtained integro-differential equation considers synaptic and space-dependent transmission delay for both general and gamma-distributed synaptic connectivities. The latter connectivity type reveals infinite, finite and vanishing self-connectivities. The work derives conditions for stationary and nonstationary instabilities for both kernel types. In addition, a nonlinear analysis for general kernels yields the order parameter equation of the Turing instability. To compare the results to findings for partial differential equations (PDEs), two typical PDE-types are derived from the examined model equation. In case of the gamma-distributed kernels, the stability conditions are formulated in terms of the mean excitatory and inhibitory interaction ranges. As a novel finding, we obtain Turing instabilities in fields with local inhibition-lateral excitation, while wave instabilities occur in fields with local excitation and lateral inhibition. Numerical simulations support the analytical results.

1 Introduction

Understanding the basic mechanisms of neural activity is supposed to yield insights to major brain functions such as cognitive processes (1), motor coordination (2) or perception (3). In addition, the understanding of pathological phenomena will support the clinical treatment of patients. Several studies in recent years indicate that some of the known pathologies represent large-scale coherent phenomena originating from mutual activity of neural populations. We mention the hand tremor in Parkinson disease (4), epileptic seizures (5) or hallucinations. For instance, the latter frequently result from specific circumstances such as fatigue or sleep deprivation (6) and, in some cases, exhibit a shift of the neural state to an instability by increased neuronal excitation (7). Ermentrout and Cowan (8) introduced a mesoscopic neuronal field theory and explained visual hallucination patterns by loss of stability at bifurcation points. Furthermore external stimuli may also evoke coherent brain activity indicating synchronous neuronal activity on a mesoscopic spatial level (9; 10; 11; 12; 3). In this context, Freeman (13) has shown in an early work that encephalographic activity relates to mesoscopic dendritic currents. Dipole and current source density models support these findings (14). These findings corroborate the study of mesoscopic models to gain further insights to brain activity.

Many works studying mesoscopic neuronal activity treat synaptically coupled neuronal ensembles (15; 16; 17; 18; 19; 20; 21; 22; 23). Our work follows the basic

field approach of Jirsa and Haken (9), who combined the ensemble models of Wilson and Cowan (24) and Nunez (25). This model considers a single type of neurons, which are interconnected by axons terminating at either excitatory or inhibitory synapses. Though the model accounts for the intrinsic delay due to axonal propagation, the delay does not affect temporal and spatial dynamics. An extended model introduces the synaptic response delay and thus adds a further time scale (26). It turns out that the relation between synaptic and propagation delay affects the stability of the system (27). This model is equivalent to the model type studied extensively by Ermentrout (8; 18; 28) and others (29; 30; 31) neglecting axonal transmission delay. Further studies considering the transmission delay revealed novel criteria for the onset of wave instabilities (26; 27; 32) and confirmed its importance to traveling phenomena (33). In addition to the temporal scales, the synaptic connectivity kernels define the spatial scales of the neuronal field. In most studies, these connectivity kernels exhibit their maximum at zero distances, i.e. strong self-connectivity.

In contrast to previous studies, the present work discusses the neural field dynamics by an analytical stability analysis for general connectivity kernels and taking into account the transmission delay. The analysis includes the derivation of the nonlinear order parameter equation for Turing instabilities and the comparison to partial differential equation models. In addition, experimental findings of Nunez (25) motivate us to focus to the family of gamma-distributed connectivity kernels, which exhibit divergent, finite, and negligible probability densities of self-connections for diverse parameters. To our best knowledge, this treatment has not been done yet in a general way. The discussion shows novel effects caused by divergent and vanishing self-connections.

The paper is organized as follows. The subsequent section presents the derivation of the field equation. In section 3, stability conditions for both stationary and non-stationary instabilities are derived analytically for general kernels, followed by the derivation of the order parameter equation of the Turing instability. In addition, the model equation is compared to partial differential equations. Finally Section 4 applies the obtained results to the case of gamma-distributed kernels, followed by numerical simulations. Section 5 summarizes the results and closes the work.

2 The model

The present work treats the well-known rate model of synaptically coupled neuronal ensembles. In the following, the model is motivated and derived from the statistics of the neuron population.

2.1 Model sections

Chemical synapses convert incoming action potentials to postsynaptic currents by emission of neurotransmitters (34). Most excitatory synapses emit neurotransmit-

ters called glutamate, which enhance the activity of the postsynaptic cells, while the neurotransmitter γ -aminobutyric (GABA) emitted by inhibitory synapses diminishes the postsynaptic cell activity. In a simplified model, synapses bind to dendrites which exhibit passive spread of current through the its tissue. According to this approach, Freeman (35) was one of the first to show that the incoming action potentials mathematically convolute with an impulse response function $h_e(t)$ and $h_i(t)$ at excitatory and inhibitory synapses, respectively. The presented approach accounts for this finding and neglects shunting effects.

In experimental practice single cell activation is measured frequently as the number of action potentials exceeding a certain threshold potential during a fixed time interval. Hence it is reasonable to discuss the mean pulse rate at time t . In addition, the model introduces spatial patches $\Gamma(x)$ at location x each containing an ensemble of synapses, that is, the activity discussed is coarse grained in space. Consequently, postsynaptic potentials averaged over time and space obey

$$\bar{V}^{e,i}(x,t) = \bar{g}_{e,i} \int_{-\infty}^t d\tau h_{e,i}(t-\tau) \bar{P}_{e,i}(x,\tau), \quad (1)$$

where $\bar{g}_{e,i}$ denote the efficacy of excitatory and inhibitory synapses and $\bar{P}_{e,i}(x,t)$ represents the presynaptic pulse rate coarse grained in time and space. The synaptic response behaviour is defined by (1) and represents the Green function for the temporal operator \hat{L} with $\hat{L}h(t) = \delta(t)$ and $\delta(t)$ being the Dirac $\delta(t)$ function.

Equation (1) assumes presynaptic pulse activity which is fast compared to the slow synaptic response. We remark that the replacement of sequences of actual spike trains is only justified if quantities relevant for the network dynamics are insensitive to trial-to-trial fluctuations, i.e. time coding of spikes is not relevant. This is given in case of uncorrelated single action potentials, which is assumed here. The introduced spatial patches $\Gamma(x)$ represent neuronal assemblies or neuronal pools (16; 24; 25; 36) which have been found experimentally both in cortical (37; 38) and subcortical (39) areas.

Essentially, we assume variations of synaptic properties in the considered neuronal population (40). Thus PSPs $V^{e,i}(t)$ at single neurons become random variables with the corresponding probability distributions $p_S^e(V^e - \bar{V}^e)$ and $p_S^i(V^i - \bar{V}^i)$. Since excitatory and inhibitory PSPs sum up at the trigger zone of each neuron (41; 33), the probability density function of the effective membrane potential $V = V^e - V^i$ is

$$p_S(V - \bar{V}) = \frac{1}{2\pi} \int dz \phi_S^e(z) \phi_S^i(-z) e^{-izV}, \quad (2)$$

where $\bar{V} = \bar{V}^e - \bar{V}^i$ and ϕ_S^e, ϕ_S^i are the characteristic functions of the corresponding probability density functions of p_S^e, p_S^i .

Now, the adjacent model section focuses on the conversion of membrane potentials to pulse activity. A single neuron generates an action potential, that is, it fires if the membrane potential $V(t)$ at the trigger zone exceeds a certain threshold V_{th} . Thus, the probability of a single neuron to fire is $\Theta(V(t) - V_{th})$, where Θ denotes

the Heaviside function. In addition, there are different types of neurons, e.g. short-range interneurons or pyramidal cells showing axonal connections on a longer range. In most cases, the former type diminishes synaptic activity, while the latter builds excitatory synaptic connections. For an ensemble of neurons at spatial location x , there is a distribution of firing thresholds $D_k(V_{th} - \bar{V}_{th}, t)$ subject to the neuron type k . Hence the expected number of firing neurons is

$$\begin{aligned} N_k(t) &= \int_{-\infty}^{\infty} dV p_S(V - \bar{V}(t)) \int_{-\infty}^{\infty} dV_{th} \Theta(V - V_{th}) D_k(V_{th} - \bar{V}_{th}, t) \\ &= \int_{-\infty}^{\infty} dw \int_{-\infty}^{w + \bar{V}(t) - \bar{V}_{th}} du p_S(w) D_k(u, t). \end{aligned}$$

where \bar{V}_{th} denotes the mean firing threshold and p_S is taken from Eq. (2). The time-averaged pulse activity at location x is given by

$$\bar{N}_k(x, t) = \int_{-\infty}^{\infty} dw \int_{-\infty}^{w + \bar{V}(x, t) - \bar{V}_{th}} du p_S(w) \bar{D}_k(u) \quad (3)$$

with the time-averaged distribution of firing thresholds $\bar{D}_k(u)$. Here, $\bar{N}_k(x, t)$ represents the average number of firing neurons of type k at time t in a neuronal ensemble at location x . Equation (3) gives the general definition of the so-called transfer function.

To be more specific, in case of normal-distributed synaptic probability distributions $p_S^{e,i}$, the effective membrane potentials obey a normal distribution $p_S \sim \mathcal{N}(0, \sigma_S^2)$. Additionally, for Gaussian-distributed firing thresholds

$$\bar{D}_k(u) = \frac{P_{max}}{\sqrt{2\pi}\sigma_k} e^{-u^2/2\sigma_k^2},$$

the transfer function and nonlinear gain read

$$\begin{aligned} \bar{N}_k(x, t) &= \frac{P_{max}}{2} (1 + \operatorname{erf}(\frac{\bar{V}(x, t) - \bar{V}_{th}}{\sqrt{2}\eta_k})) = P_{max} S_k(V(x, t)) \quad (4) \\ \frac{\partial \bar{N}_k(x, t)}{\partial \bar{V}} &= \frac{P_{max}}{\sqrt{2\pi}\eta_k} e^{-(\bar{V}(x, t) - \bar{V}_{th})^2/2\eta_k^2}, \end{aligned}$$

respectively, where $\eta_k^2 = \sigma_S^2 + \sigma_k^2$, $\operatorname{erf}(x)$ represents the Gaussian error function and P_{max} denotes the maximum firing rate. By virtue of the probabilistic origin of $\bar{N}_k(x, t)$, it owns a sigmoidal shape and the corresponding nonlinear gain reveals a maximum $P_{max}/(\sqrt{2\pi}\eta_k)$. Equation (4) shows accordance to previous results (42) for a single neuron type.

Finally, the model field contains axonal fibres linking trigger zones and dendritic structures of terminal neurons. With the probabilities of excitatory and inhibitory axonal connections $K_e(x, y)$ and $K_i(x, y)$, respectively, the nonlocal interactions

yield temporal propagation delays in case of finite axonal propagation speeds v_e and v_i . Hence, the presynaptic pulse activity reads

$$\bar{P}_{e,i}(x, t) = \int_V dx' K_{e,i}(x, x') \bar{N}_k(x', t - \frac{|x - x'|}{v_{e,i}}) + \mu_{e,i} I(x, t) \quad (5)$$

with coupling factors $\mu_{e,i}$. The additional pulse activity $I(x, t)$ introduces an external input, e.g. from other cortical regions or from the midbrain (25).

2.2 The field equation

Combining the previous results, the evolution equation reads

$$\begin{aligned} \hat{L}V(x, t) = & \int_{-\infty}^{\infty} a_e K_e(x - y) S_e(V(y, t - \frac{|x - y|}{v_e})) \\ & - a_i K_i(x - y) S_i(V(y, t - \frac{|x - y|}{v_i})) dy + \mu I(x, t) \end{aligned} \quad (6)$$

with $a_{e,i} = \bar{g}_{e,i} P_{\max}$ and $\mu = \mu_e - \mu_i$. Equation (6) accounts for two types of neurons, namely excitatory pyramidal cells $k = e$ and inhibitory stellate cells $k = i$.

3 Analysis for general kernels

This section aims to study the stability of a stationary state V_0 which is constant in space. Here, we choose one type of neuron $S_e = S_i = S$ and specify the impulse response function to $h(t) = \alpha_1 \alpha_2 / (\alpha_2 - \alpha_1) (\exp(-\alpha_1 t) - \exp(-\alpha_2 t)) \Theta(t)$. After rescaling time to $t \rightarrow t \sqrt{\alpha_1 \alpha_2}$, the temporal operator reads

$$\hat{L} = \left(\frac{\partial^2}{\partial t^2} + \gamma \frac{\partial}{\partial t} + 1 \right) \quad (7)$$

with $\gamma = \alpha_1 / \alpha_2 + \alpha_2 / \alpha_1 \geq 2$. In case of constant external input $\mu I(x, t) = I_0$, Eq. (6) gives the implicit equation for the stationary state $V(x, t) = V_0$ as

$$V_0 = (a_e - a_i) S(V_0) + I_0. \quad (8)$$

and Fig. 1 illustrates its different solutions for $a_e > a_i$ with respect to I_0 as external control parameter. We mention the similarity to a cusp catastrophe (43).

For deviations $u(x, t) = V(x, t) - V_0 = u_0 e^{\lambda t + i k x}$, the characteristic equation reads

$$L(\lambda) = s \int_{-\infty}^{\infty} dz \left(a_e K_e(z) e^{-\frac{\lambda}{v_e} |z|} - a_i K_i(z) e^{-\frac{\lambda}{v_i} |z|} \right) e^{-i k z} \quad (9)$$

with the nonlinear gain $s = \delta S / \delta V$ at $V = V_0$. Here and in the following, $\delta / \delta V$ denotes the functional derivative. Since I_0 determines V_0 and s , the nonlinear gain represents the control parameter in the following.

When $s = 0$, one has $L(\lambda) = \lambda^2 + \gamma\lambda + 1 = 0$, so that $\text{Re } \lambda < 0$ and the perturbations u are damped out. It follows that V_0 is asymptotically stable for all small s , since the values (λ, k) satisfying the dispersion relation (9) depend continuously on s . However, increasing s further may result in a loss of stability; in this critical transition one has $\text{Re } \lambda = 0$. Thus setting $\lambda = i\omega$ for some $\omega \in \mathbf{R}$ in (9), we get

$$1 - \omega^2 + i\omega\gamma = s \int_{-\infty}^{\infty} dz (a_e K_e(z) e^{-i\omega|z|/v_e} - a_i K_i(z) e^{-i\omega|z|/v_i}) e^{ikz}. \quad (10)$$

Comparing the magnitudes of both sides,

$$\sqrt{(1 - \omega^2)^2 + \gamma^2 \omega^2} \leq s \int_{-\infty}^{\infty} dz (a_e |K_e(z)| + a_i |K_i(z)|). \quad (11)$$

By simple calculus and the fact that $\gamma \geq 2$,

$$(1 - \omega^2)^2 + \gamma^2 \omega^2 \geq 1 \quad \text{for all } \omega \in \mathbf{R}. \quad (12)$$

Also by definition (cf. section 2.1)

$$\int_{-\infty}^{\infty} dz |K_{e,i}(z)| = 1. \quad (13)$$

Using (12) and (13) in (11), we obtain the necessary condition for loss of stability

$$1 \leq s(a_e + a_i). \quad (14)$$

Hence, the stationary state V_0 is asymptotically stable for $s < 1/(a_e + a_i)$. In order to investigate the dynamics of the nonlinear equation (6), it is useful to classify the different ways in which V_0 may lose its stability subject to the parameter s .

3.1 Stationary instability

For stationary bifurcations, $\omega = 0$ and the threshold for s becomes

$$s_c = \frac{1}{a_e \hat{K}_e(k_c) - a_i \hat{K}_i(k_c)} = \frac{1}{\hat{K}(k_c)}, \quad k_c = \arg \min_k \hat{K}(k) \quad (15)$$

where \hat{K}_e and \hat{K}_i are the Fourier transforms, i.e. the characteristic functions, of the connectivity probability densities K_e and K_i , respectively.

In case of a constant bifurcation, the stationary state loses stability for

$$s > \frac{1}{\hat{K}(0)} = \frac{1}{a_e - a_i}. \quad (16)$$

Figure 2 shows the corresponding bifurcation diagram for various parameters a_e, a_i . As mentioned in Section 2.1, the nonlinear gain s is constrained from above by

$s_m = 1/(\sqrt{2\pi}\eta)$. It follows, that if $s_m < 1/(a_e - a_i)$ holds all stationary solutions are stable with respect to constant bifurcations.

However, increasing s from zero, a non-constant bifurcation may emerge for $\hat{K}(k) > \hat{K}(0)$ and $(a_e + a_i) > \hat{K}(k_c) > (a_e - a_i)$ with $k_c \neq 0$ and $a_e > a_i$. That is, Eq. (15) represents the condition for the instability onset with $k \neq 0$. The corresponding bifurcation has been found first by Turing in non-equilibrium activator-inhibitor systems (44; 45). As mentioned in Section 2.1, the nonlinear gain s is constraint from above with maximum $s_m = 1/(\sqrt{2\pi}\eta)$. Subsequently, Turing bifurcations might occur only if $\hat{K}(k_c) > 1/s_m \sim \eta$, i.e. in case of small statistical variances of membrane potentials and firing thresholds. This additional condition relates the statistical field properties directly with the macroscopic behaviour.

3.2 Non-stationary instability

This type of bifurcation is characterized by a solution pair (λ, k) of (9) with $\lambda = i\omega \neq 0$. We shall show that such bifurcations are possible only if the transmission speeds $v_{e,i}$ are sufficiently small, and obtain an estimate to quantify this statement.

Considering the imaginary part of (10),

$$\begin{aligned} \omega\gamma &= -s \int_{-\infty}^{\infty} dz (a_e K_e(z) \sin(\omega|z|/v_e) - a_i K_i(z) \sin(\omega|z|/v_i)) \cos(kz) \\ &\quad + s \int_{-\infty}^{\infty} dz (a_e K_e(z) \cos(\omega|z|/v_e) - a_i K_i(z) \cos(\omega|z|/v_i)) \sin(kz). \end{aligned}$$

Note that the integrand in the first integral is an even function of z while that in the second integral is an odd function. Thus the second integral vanishes, and we have

$$\omega\gamma = -2s \int_0^{\infty} dz (a_e K_e(z) \sin(\omega z/v_e) - a_i K_i(z) \sin(\omega z/v_i)) \cos(kz)$$

which yields

$$|\omega|\gamma \leq 2s \int_0^{\infty} dz (a_e |K_e(z) \sin(\omega z/v_e)| + a_i |K_i(z) \sin(\omega z/v_i)|).$$

Using the fact that $|\sin x| \leq |x|$ for all x , we obtain

$$|\omega|\gamma \leq 2s \int_0^{\infty} dz (a_e |K_e(z) \omega z/v_e| + a_i |K_i(z) \omega z/v_i|)$$

and since $\omega \neq 0$ at a non-stationary bifurcation,

$$\gamma \leq s \left(\frac{a_e}{v_e} \int_0^{\infty} dz 2K_e(z)z + \frac{a_i}{v_i} \int_0^{\infty} dz 2K_i(z)z \right).$$

Note that the integrals are the definitions of the mean spatial interaction ranges

$$\xi_e = \int_{-\infty}^{\infty} dz |z| K_e(z) \quad , \quad \xi_i = \int_{-\infty}^{\infty} dz |z| K_i(z) \quad (17)$$

for excitatory and inhibitory connections. Hence we define $\tau_e = \xi_e/v_e$ and $\tau_i = \xi_i/v_i$ as the mean delay times respectively for the excitatory and inhibitory information transmission in the field. In this way, we can express a necessary condition for non-stationary bifurcations to occur, namely

$$s \geq s_c = \frac{\gamma}{a_e\tau_e + a_i\tau_i}. \quad (18)$$

Since all quantities are positive, it is clear that at least one of the velocities v_e or v_i must be finite for the occurrence of non-stationary bifurcations. A similar condition is derived in (27) for the case $v_e = v_i$. This result generalizes in some aspects previous results of Crook et al. (32) for networks of coupled oscillators. They revealed the importance of the ratio between spatial excitatory range and transmission speed for exponential kernels in context of the oscillation stability.

With Eq. (18) and the previous condition $1/(a_e + a_i) < s < 1/(a_e - a_i)$ for non-constant bifurcations, the parameter regime for nonstationary bifurcation is given by

$$\frac{\gamma}{\tau_e \frac{a_e}{a_i} + \tau_i} < a_i s < \frac{1}{\frac{a_e}{a_i} - 1} \quad , \quad \frac{1}{\frac{a_e}{a_i} + 1} < a_i s$$

As can be shown by simple calculus, there is a threshold

$$a_e/a_i = \frac{\gamma + \tau_i}{\gamma - \tau_e} \quad , \quad \tau_e < \gamma$$

beyond which no nonstationary bifurcations occur, while $\tau_e > \gamma$ allows nonstationary bifurcations for all $a_e/a_i \geq 1$. Figure 3 illustrates these findings.

Finally, we apply an asymptotic analysis for large transmission speeds $v_{e,i}$. Let us consider the integral

$$\begin{aligned} \int_{-\infty}^{\infty} dz K(z) e^{-ikz} e^{-\lambda|z|/v} &= \int_{-\infty}^{\infty} dz K(z) e^{-ikz} \sum_{n=0}^{\infty} \frac{1}{n!} (-\lambda|z|/v)^n \\ &= \sum_{n=0}^{\infty} \frac{1}{n!} \int_{-\infty}^{\infty} dz K(z) |z|^n e^{-ikz} (-\lambda\epsilon)^n \\ &= \sum_{n=0}^{\infty} \frac{1}{n!} (-\lambda\epsilon)^n \hat{K}_n(k) \end{aligned}$$

with

$$\hat{K}_n(k) = \int_{-\infty}^{\infty} dz |z|^n K(z) e^{-ikz} = 2 \int_0^{\infty} dz z^n K(z) \cos(kz)$$

and $\epsilon = 1/v$. We use this series expansion in the characteristic equation (9), where, in case of local inhibitory and long-range excitatory connections, the delay due to inhibitory connections is neglected, i.e. $1/v_i = 0$. For excitatory and inhibitory

kernels, large transmission speed v_e and $\lambda = i\omega$, we set $1/v_e = \epsilon$ and obtain by neglecting higher order terms $\epsilon^n \forall n > 2$

$$L(i\omega) \approx s\hat{K}(k) - i\omega a_e s \hat{K}_1^e(k)\epsilon - a_e \frac{\omega^2 s}{2} \hat{K}_2^e(k)\epsilon^2.$$

After separating real and imaginary part, we get

$$s_{co} = -\frac{\gamma}{a_e \epsilon \hat{K}_1^e(k^*)}, \quad \Omega^2 = 2 \frac{s_{co} \hat{K}(k^*) - 1}{a_e s_{co} \epsilon^2 \hat{K}_2^e(k^*) - 2} \quad (19)$$

That is, increasing s from zero the Hopf instability sets in at s_{co} with wave number k^* . In case of $k^* = 0$, the emerging pattern exhibits global in-phase oscillations with oscillation frequency Ω , while $k^* \neq 0$ yields wave-like phenomena with phase speed $v_{ph} = \omega/k^*$.

3.3 Nonlinear analysis of the Turing instability

Now in order to learn something about the nonlinear behaviour near the bifurcation point, this section aims at the nonlinear amplitude equation of the Turing instability. As showed in the previous examinations, the Turing bifurcation does not depend on the transmission speeds and thus it is $v_e, v_i \rightarrow \infty$ in this section.

Expanding Eq. (6) to cubic nonlinear order about V_0 , it is

$$\begin{aligned} \hat{L}V(x, t) &= \int_{-\infty}^{\infty} dy K(x-y) S(V(y, t)) + I_0 \\ \hat{L}u(x, t) &\approx \int_{-\infty}^{\infty} dy K(x-y) [su(y, t) + \beta u^2(y, t) + \epsilon u^3(y, t)] \end{aligned} \quad (20)$$

with $K = a_e K_e - a_i K_i$ and $\beta = (\delta^2/\delta V^2)/2$, $\epsilon = (\delta^3/\delta V^3)/6$ computed at $V = V_0$.

Now, we expand the field by the spatial eigenfunctions of the linear problem

$$u(x, t) = \int_{-\infty}^{\infty} dk \xi(k, t) e^{ikx} \quad (21)$$

with amplitudes $\xi(k, t) = \xi^*(-k, t)$ and $*$ denotes the complex conjugate. In the following, $\xi(k, t)$ is abbreviated to $\xi(k)$ for simplicity, while it remains time-dependent.

Inserting (21) to (20) and integrating both sides over the space domain, we have

$$\begin{aligned}
\hat{L}\xi(k) &= \frac{1}{2\pi} \int_{-\infty}^{\infty} dx e^{-ikx} [s \int_{-\infty}^{\infty} dk_1 \int_{-\infty}^{\infty} dy K(x-y) e^{ik_1 y} \xi(k_1) \\
&\quad + \beta \int_{-\infty}^{\infty} dk_1 \int_{-\infty}^{\infty} dk_2 \int_{-\infty}^{\infty} dy K(x-y) e^{iy(k_1+k_2)} \xi(k_1) \xi(k_2) \\
&\quad + \epsilon \int_{-\infty}^{\infty} dk_1 \int_{-\infty}^{\infty} dk_2 \int_{-\infty}^{\infty} dk_3 \int_{-\infty}^{\infty} dy K(x-y) e^{iy(k_1+k_2+k_3)} \xi(k_1) \xi(k_2) \xi(k_3)] \\
&= \frac{1}{2\pi} \int_{-\infty}^{\infty} dx e^{-ikx} [s \int_{-\infty}^{\infty} dk_1 \hat{K}(k_1) e^{ik_1 x} \xi(k_1) \\
&\quad + \beta \int_{-\infty}^{\infty} dk_1 \int_{-\infty}^{\infty} dk_2 \hat{K}(k_1+k_2) e^{ix(k_1+k_2)} \xi(k_1) \xi(k_2) \\
&\quad + \epsilon \int_{-\infty}^{\infty} dk_1 \int_{-\infty}^{\infty} dk_2 \int_{-\infty}^{\infty} dk_3 \hat{K}(k_1+k_2+k_3) e^{ix(k_1+k_2+k_3)} \xi(k_1) \xi(k_2) \xi(k_3)] \\
\hat{L}\xi(k) &= s\hat{K}\xi(k) + \beta\hat{K}(k) \int_{-\infty}^{\infty} dk_1 \xi(k_1) \xi(k-k_1) \\
&\quad + \epsilon\hat{K}(k) \int_{-\infty}^{\infty} dk_1 \int_{-\infty}^{\infty} dk_2 \xi(k_1) \xi(k_2) \xi(k-k_1-k_2)] \tag{22}
\end{aligned}$$

Since \hat{L} is a temporal differential operator of second order, we write Eq. (22) as a system of two first-order differential equations

$$\dot{\xi}(k) = \eta(k) \tag{23}$$

$$\dot{\eta}(k) = (-1 + s\hat{K})\xi(k) - \gamma\eta(k) + N(\xi(k)), \tag{24}$$

while $N(\cdot)$ represents the nonlinear terms in Eq. (22). Now, we transform this equation system to a coordinate system with diagonal linear part by $\mathbf{x}(k) = \mathbf{P}(k)\mathbf{y}(k)$, where $\mathbf{x}(k) = (\eta(k), \xi(k))^t$ and $\mathbf{P}(k)$ is the 2×2 transformation matrix. It follows

$$\dot{\mathbf{y}}(k) = \mathbf{D}(k)\mathbf{y} + \mathbf{P}^{-1}(k)\mathbf{n}(\mathbf{y}(k)), \tag{25}$$

while $\mathbf{n} = (0, N(\mathbf{y}))^t$, $\mathbf{D}(k) = \mathbf{P}^{-1}(k)\mathbf{A}(k)\mathbf{P}(k)$ is a 2×2 matrix and $\mathbf{A}(k)$ represents the linear matrix in the system (23)-(24). The matrix \mathbf{D} is diagonal, if the columns of \mathbf{P} contain the eigenvectors of matrix \mathbf{A} . The eigenvalues of \mathbf{A} are

$$\alpha(k) = \frac{1}{2}(-\gamma + \sqrt{\gamma^2 + 4(-1 + s\hat{K}(k))}), \tag{26}$$

$$\delta(k) = \frac{1}{2}(-\gamma - \sqrt{\gamma^2 + 4(-1 + s\hat{K}(k))}) < 0 \tag{27}$$

with corresponding eigenvectors $\mathbf{v}(k) = (1, \alpha(k))^t$ and $\mathbf{w}(k) = (1, \delta(k))^t$. Since $\alpha(k)$, $\delta(k)$ are real and $\det \mathbf{P}(k) \neq 0$ for all k , the coordinate transformation by $\mathbf{P}(k)$ is valid. Thus the transformed differential equation system (23)-(24) reads

$$\dot{y}_1(k) = \alpha(k)y_1(k) - N(\mathbf{y}(k)) \tag{28}$$

$$\dot{y}_2(k) = \delta(k)y_2(k) + N(\mathbf{y}(k)) \tag{29}$$

with $\mathbf{y} = (y_1, y_2)^t$. Hence by virtue of the properties of $\alpha(k)$ and $\delta(k)$, the modes $y_2(k)$ are stable for all k , while $y_1(k)$ are stable for $(k - k_c)/k_c \gg 1$. In contrast $y_1(k)$ evolves on a much larger time scale near the Turing threshold $s\hat{K}(k) = 1$, i.e. $k \approx k_c$ (cf. Eq.(15)). In the following, the latter modes are denoted $z(k)$, while the stable modes $y_1(k)$ are renamed to $s(k)$. According the center manifold theorem (46) $z(k)$ evolves on a center manifold, while the other modes obey $y_2(k) = f_k(z(k))$ and $s(k) = g_k(z(k))$ for some functions f_k, g_k . In more physical terms, the present separation of time scales near the bifurcation threshold yields a slaving mechanism and a circular causality (47). That is the modes $z(k)$ slave $y_2(k)$ and $s(k)$, while these slaved modes also determine the evolution of $z(k)$.

Now, we approximate $f_k(z(k))$ and $g_k(z(k))$ to lowest nonlinear orders and expand the nonlinear term in (28) to cubic polynomial order in z . Applying the introduced coordinate transformation $\xi = y_1 + y_2$,

$$\dot{y}_2(k) = \delta(k)y_2(k) + \beta\hat{K}(k) \int_{-\infty}^{\infty} dk' z(k')z(k - k') \quad (30)$$

$$\dot{s}(k) = \alpha(k)s(k) - \beta\hat{K}(k) \int_{-\infty}^{\infty} dk' z(k')z(k - k') \quad (31)$$

$$\begin{aligned} \dot{z}(k) = & \alpha(k)z(k) - \beta\hat{K}(k) \int_{-\infty}^{\infty} dk' [z(k')z(k - k') + z(k')s(k - k') \\ & + s(k')z(k - k') + z(k')y_2(k - k') + y_2(k')z(k - k')] \\ & + \epsilon\hat{K}(k) \int_{-\infty}^{\infty} dk' \int_{-\infty}^{\infty} dk'' z(k'')z(k')z(k - k' - k'') \end{aligned} \quad (32)$$

Essentially after adiabatic elimination in Eq. (30) and (31) and inserting the results to Eq. (32), we find the order parameter equation

$$\dot{z}(k) = \alpha(k, s)z(k) + \Pi(k, s)z^3(k) \quad \forall k \approx k_c \quad (33)$$

by utilizing $z(k) = z(-k)$. In addition,

$$\Pi(k, s) = \hat{K}(k) [C\beta^2(s) + \epsilon(s)] \quad (34)$$

$$C = 2\hat{K}(0)\left(\frac{1}{\delta(0)} - \frac{1}{\alpha(0)}\right) + \hat{K}(2k_c)\left(\frac{1}{\delta(2k_c)} - \frac{1}{\alpha(2k_c)}\right) > 0. \quad (35)$$

In contrast to standard bifurcation theory, here both α and Π depend on the control parameter s .

Now recall that the general Turing instability exhibits stable stationary points $z_{st} > 0$ for $s > s_c$ due to nonlinear saturation, that is $\Pi < 0$. Figure 4 shows plots of β^2 and ϵ with respect to the control parameter s . It turns out that $\Pi < 0$ and thus $\epsilon < 0$ only if s exceeds a certain threshold. In this case, Eq. (33) describes the supercritical pitchfork bifurcation with the necessary nonlinear saturation. In contrast $\Pi > 0$ yields no stable stationary solutions $z_s > 0$ and both the applied quadratic approximations for the modes $y_2(k)$ and $s(k)$ and the adiabatic elimination

procedure turn out being insufficient. That is, higher order polynomials need to be discussed. However, in the following we focus to the case of $\Pi < 0$.

Figure 5 presents plots of Π with respect to the bifurcation thresholds s_c for some ξ_e, ξ_i . For $\Pi(s_c) < 0$, pitchfork bifurcations occur at $s \approx s_c$. Figure 6 shows the bifurcation diagram of the stationary solution z_{st} with respect to α (right panel) with $z_{st} = \sqrt{\alpha(s)/[\hat{K}(k)(C\beta^2(s) + \epsilon(s))]}$. The corresponding potential $V_{pot}(z)$ with $\dot{z} = -dV_{pot}/dz$ is plotted in Fig. 6(left panel) for some control parameter s .

3.4 Comparison to partial differential equations

The integro-differential equation (6) accounts for long-range interaction. To investigate its relation to partial differential equations (PDEs), we re-write the integral as

$$\begin{aligned} \int_{-\infty}^{\infty} dy K(x-y) S(V(y)) &= \int_{-\infty}^{\infty} d\eta K(\eta) S(V(x-\eta)) \\ &= \int_{-\infty}^{\infty} d\eta K(\eta) \sum_{n=0}^{\infty} (-1)^n \frac{1}{n!} \frac{\partial^n S(V(x-\eta))}{\partial(x-\eta)^n} \Big|_{x-\eta=x} \eta^n \\ &= \sum_{n=0}^{\infty} (-1)^n K_n \frac{\partial^n S(V(x))}{\partial x^n} \end{aligned}$$

with the kernel moments $K_n = \int d\eta K(\eta) \eta^n \forall n \in \mathbf{N}$. In the present work, the kernels are symmetric and thus $K_n = 0$ for odd orders n . Then we find

$$\begin{aligned} \int_{-\infty}^{\infty} dy K(x-y) S(V(y)) &\approx K_0 S(V(x)) + K_2 \frac{\delta S^2}{\delta V^2} \left(\frac{\partial V}{\partial x} \right)^2 + K_4 \frac{\delta^4 S}{\delta V^4} \left(\frac{\partial V}{\partial x} \right)^4 \\ &\quad + K_2 \frac{\delta S}{\delta V} \frac{\partial^2 V}{\partial x^2} + 6K_4 \frac{\delta^3 S}{\delta V^3} \left(\frac{\partial V}{\partial x} \right)^2 \frac{\partial^2 V}{\partial x^2} \\ &\quad + 3K_4 \frac{\delta^2 S}{\delta V^2} \left(\frac{\partial^2 V}{\partial x^2} \right)^2 + 4K_4 \frac{\delta^2 S}{\delta V^2} \frac{\partial V}{\partial x} \frac{\partial^3 V}{\partial x^3} \\ &\quad + K_4 \frac{\delta S}{\delta V} \frac{\partial^4 V}{\partial x^4} \end{aligned} \tag{36}$$

Now, we distinguish between different neuron types as introduced in Section 2.1. In the following, K_n^e and K_n^i denote kernel moments for excitatory and inhibitory interactions, respectively. First, let us assume excitatory neurons which exhibit short but non-vanishing interaction, while inhibitory connections are local only. In case of $S_i \gg S_e$, the transfer function S_e for excitatory neurons expands to linear polynomial order about a fixed V_0 . In case of the first-order operator \hat{L} and short

range excitation $K_{2n}^e \rightarrow 0 \forall n > 1$, we obtain

$$\begin{aligned} \left(\frac{\partial u}{\partial t} + 1\right)u(x, t) &\approx K_0^e S_e(V_0) + sK_0^e u(x, t) + sK_2^e \frac{\partial^2 u}{\partial x^2} \\ &\quad - K_0^i S_i(u(x) + V_0) \\ \frac{\partial u}{\partial t} u(x, t) &= f(u(x), s, V_0) + D \frac{\partial^2 u}{\partial x^2} \end{aligned} \quad (37)$$

with $s = \delta S_e / \delta V$ and the polynomial $f(u)$. Equation (37) represent a reaction-diffusion equation with the diffusion coefficient $D = sK_2^e$.

In case of longer excitatory interaction with $K_{2n}^e \rightarrow 0 \forall n > 2$, while expanding the transfer functions S_e and S_i to linear and third polynomial order about V_0 , respectively, we get

$$\begin{aligned} \left(\frac{\partial u}{\partial t} + 1\right)u(x, t) &\approx K_0^e S(V_0) + sK_0^e u(x, t) + sK_2^e \frac{\partial^2 u}{\partial x^2} + sK_4^e \frac{\partial^4 u}{\partial x^4} \\ &\quad - (K_0^i S(V_0) + sK_0^i u(x, t) + \beta K_0^i u^2(x, t) + \epsilon K_0^i u^3(x, t)) \end{aligned}$$

and finally after an affine transformation and scaling of time

$$\frac{\partial u}{\partial t} u(x, t) = \beta_1 u(x, t) - \beta_2 u^3(x, t) + \beta_3 e \frac{\partial^2 u}{\partial x^2} + \frac{\partial^4 u}{\partial x^4}. \quad (38)$$

This PDE is a variant of the well-known Swift-Hohenberg equation (48; 49).

4 Gamma-distributed kernels

In most previous works (8; 26; 50), neuronal fields exhibit axonal connections which are maximal at zero distance and monotonically decreasing for increasing distance. Then, the combination of excitatory and inhibitory axonal networks may yield four different spatial interactions, namely pure excitation, pure inhibition, local excitation-lateral inhibition and local inhibition-lateral excitation. In contrast, the current work picks up an interesting result of Nunez (25), who estimated the distribution of axonal cortico-cortical fiber lengths in humans based on distributions in mice. He found that cortico-cortical, i.e. excitatory, connections in humans may obey a gamma distribution with maximum at some centimeters. A similar problem has been addressed by Rinzel et al. (51), who found new propagation patterns in inhibitory networks with vanishing self-connections. Since there is also strong anatomical evidence for self-connections in inhibitory networks in cat visual cortex (52), we set the corresponding axonal distribution to a decreasing exponential.

4.1 Field properties

For gamma distributed connections, the connection probabilities read

$$K_e(x, y) = \frac{1}{2r_e^p \Gamma(p)} |x - y|^{p-1} e^{-|x-y|/r_e}, \quad K_i(x, y) = \frac{1}{2r_i} e^{-|x-y|/r_i} \quad (39)$$

where $p > 0$ is a parameter of the gamma distribution, $\Gamma(p)$ denotes the gamma function and r_e, r_i are the spatial ranges of excitatory and inhibitory connectivity kernels, respectively. After scaling $t \rightarrow t\sqrt{\alpha_1\alpha_2}, x \rightarrow x/r_e, v_{e,i} \rightarrow v_{e,i}/(r_e\sqrt{\alpha_1\alpha_2})$, we get

$$K_e(x) = \frac{1}{2\Gamma(\xi_e)}|x|^{\xi_e-1}e^{-|x|}, \quad K_i(x) = \frac{1}{2\xi_i}e^{|x|/\xi_i}, \quad (40)$$

with $\xi_e = p, \xi_i = r_i/r_e$ taken from (17). The temporal operator \hat{L} is taken from section 3, and furthermore $S_e = S_i = S$.

In most studies treating spatial structures in neuronal fields, excitatory and inhibitory connectivity kernels are of the same functional type such as exponentials or Gaussians. In these models, the excitation and inhibition comes in by different spatial scales, say r_e, r_i . In consequence, the spatial interaction ranges can be scaled to $\xi_e = 1$ and $\xi_i \neq 1$. That is, the single parameter ξ_i reflects the relation of the excitatory and the inhibitory spatial scale and thus defines the spatial interaction. In contrast, Eq. (39) introduces the additional parameter p yielding two variables. Now $\xi_i \neq 1$ still gives the relation of excitation and inhibition, while ξ_e is related to the excitatory self-interaction.

To be more precise, Figure 7 shows both kernels for various parameters ξ_e, ξ_i and we observe singular self-excitations for $\xi_e < 1$ (Fig. 7, left panel). At a first glance, this singularity of the probability density K_e may appear unphysical. However, this effect occurs even in much more simple processes and we mention the standard Brownian motion exhibiting a singular probability density of sojourn times (53; 54). In addition, $\xi_e > 1$ leads to $K_e(0) = 0$, while the maximum of $K_e(x)$ is located at $x_0 = \xi_e - 1$. That is the self-excitation vanishes and the maximum connectivity is reached at the distance x_0 from the origin. Subsequently by considering the inhibitory kernel, $\xi_e < 1$ yields local inhibition with the self-interaction $a_e K_e(0) - a_i K_i(0) = -a_i/\xi_i^2$ for all ξ_i and $a_e, a_i > 0$, while $\xi_e > 1$ reflects local excitations for all ξ_i and $a_e, a_i > 0$. These cases contrast to the well-known case $\xi_e = 1$, which facilitates both local excitation and inhibition subject to a_e/a_i and ξ_i .

4.2 Stationary instability

For the special choice of kernels (40), the condition for the Turing instability (15) reads $s_c = 1/\hat{K}(k_c)$ with

$$\hat{K}(k) = \frac{a_e}{\sqrt{1+k^2}^{\xi_e}} \cos(\xi_e \arctan(k)) - \frac{a_i}{1+\xi_i^2 k^2}.$$

Since $s_c > 0$ and $\hat{K}(k) \rightarrow 0$ as $k \rightarrow \infty$, $\hat{K}(k_c)$ represents a positive local maximum for finite k_c . The corresponding sufficient condition reads

$$\frac{\partial^2 \hat{K}(k)}{\partial k^2} \Big|_{k=0} > 0 \Rightarrow \xi_i^2 > \frac{a_e}{2a_i} \xi_e (\xi_e + 1) \quad (41)$$

with

$$\frac{\partial^2 \hat{K}(k)}{\partial k^2} = -\frac{a_e \xi_e (\xi_e + 1)}{\sqrt{1 + k^2}^{\xi_e + 2}} \cos((\xi_e + 2) \arctan(k)) + 2a_i \xi_i^2 \frac{1 - 3\xi_i^2 k^2}{(1 + \xi_i^2 k^2)^3}.$$

Figure 8 shows the corresponding parameter space.

In case of $a_e > a_i$ and $\xi_e < 1$, Turing patterns occur only for $\xi_i > \xi_e$ (Fig. 9), i.e. for larger mean inhibitory interaction than mean excitatory interaction. This behaviour shows accordance to previous findings. However, for $\xi_i < \xi_e$ we find also Turing instabilities with the additional condition $\xi_e \geq (a_e/a_i)/(2 - a_e/a_i)$. That is Turing patterns occur even for local inhibitory interactions, which has not been found in previous works. In case of $a_e < a_i$, Turing patterns might also occur for $\xi_i < \xi_e$ and $\xi_e \geq (a_e/a_i)/(2 - a_e/a_i)$.

Figure 10 shows the effective kernel $a_e K_e(x) - a_i K_i(x)$ and corresponding Fourier transform $\hat{K}(k)$ for both $\xi_e = 1$ and $\xi_e = 2.0$. We observe that the kernels exhibit local excitation-lateral inhibition interaction with $\xi_e = 1$, while for $\xi_i > 1$ Turing instabilities may also occur for $\xi_e = 2$ although the kernel elicits local inhibition-lateral excitation interaction. Eventually recalling the findings of Nunez (25), experiments indicate intracortical inhibitory connections with $r_i \approx 1\text{mm}$ and cortico-cortical connections with $r_e = 20\text{mm}$, that is $\xi_i = 0.05$. In addition, $a_e > a_i$ and $\xi_e = 3$. Subsequently, according to Eq. (41) and Fig. 8, Turing patterns do not occur for these parameters and have not been found in experiments yet.

4.3 Non-stationary instability

According to section 3.2, the bifurcation threshold s_{co} for oscillatory instabilities depends strongly on the kernel Fourier moments \hat{K}_m . These moments read for kernels (40)

$$\begin{aligned} \hat{K}_m^e(k) &= \frac{\Gamma(\xi_e + m)}{\Gamma(\xi_e) \sqrt{1 + k^2}^{(\xi_e + m)}} \cos((\xi_e + m) \arctan(k)) \\ \hat{K}_m^i(k) &= \frac{\Gamma(m + 1) \xi_i^m}{\sqrt{1 + k^2}^{(m + 1)}} \cos((m + 1) \arctan(\xi_i k)). \end{aligned}$$

Figure 11 shows plots of v_{ph} with respect to v_e for various ξ_e, ξ_i . We point out that the phase speed is smaller than the transmission speed in accordance to previous experimental (55) and theoretical results (26; 27). In contrast to previous findings, there are also oscillatory instabilities for $\xi_e < 1$, i.e. local excitation-lateral inhibition fields.

4.4 Numerical simulation

For the numerical investigations, Eq. (4) is approximated by the logistic function $\bar{N} = P_{\max}/(1 + \exp(-1.8(V - 3.0)))$ (56). The synaptic parameters are set to

$\alpha_1/\alpha_2 = 1.46$ i.e. $\gamma = 2.1$, while the propagation speed along excitatory axonal connections is set to $v_e = 10$ and the delay corresponding to short-range inhibitory connections is neglected. The subsequent temporal integration procedure applies an Euler algorithm while the spatial integration algorithm represents an adaptive integration procedure. This algorithm divides the integration region into subintervals, and on each iteration the subinterval with the largest estimated error is bisected. Each interval is integrated according to the 61 point Gauss-Kronrod rules (57). Further, periodic boundary conditions are set yielding the integration rule

$$\int_{-\infty}^{\infty} K(|x-y|)f(y)dy \approx \int_0^L K(L/2 - |L/2 - |x-y||)f(y)dy.$$

with $L = Ndx$.

The first simulation aims to verify the Turing instability found analytically in section (3.3). Figure 12 presents the Turing instability by a space-time plot for initial values $V^0(x, t) = V_0 + 0.5(\cos(0.5k_c x) + \cos(k_c x) + \cos(2.0k_c x))$ for $L/v_e \leq t \leq 0$ with the critical wave number k_c .

Finally to verify the novel findings of the previous section, we simulate the field activity for $\xi_e = 2.0$ and $\xi_i = 1.92$ with the same initial conditions. Figure 13 presents the corresponding space-time plot, which confirms the Turing instability for local inhibition-lateral excitation fields.

5 Conclusion

The present work derives the neural model from statistical neural properties and analyses the integro-differential equation with respect to its stability. The first part of the analysis gives conditions for stationary and non-stationary instabilities. It is shown that the stationary bifurcation threshold is independent of the transmission speed and defined mainly by the Fourier transforms of the excitatory and inhibitory connectivity kernel. This result yields the condition for the onset of Turing instabilities. In turn, the non-stationary bifurcations strongly depend on the mean interaction time of excitatory and inhibitory connections, where the interaction time represents the ratio of mean interaction range to transmission speed. Furthermore, a perturbation analysis for large transmission speeds yields the bifurcation threshold for Hopf-instabilities, the corresponding wave number, and the phase velocity of the emerging wave instabilities. Here, the bifurcation threshold depends mainly on the excitatory and inhibitory kernel Fourier moments. To gain further information on the existence of instabilities, the order parameter equation for Turing patterns is derived and discussed in some detail. A subsequent comparison of the model to partial differential equations reveal the relation to reaction-diffusion models and the Swift-Hohenberg equation. Finally, applications to the gamma-distributed excitatory kernels reveal Turing instabilities for local inhibition-lateral excitation fields and wave instabilities for local excitation-lateral inhibition fields. These novel

findings contrast previous results and originate from the divergent and vanishing self-connection, respectively.

The presented study aims to generalize the analysis of non-locally interacting neural fields in order to gain a classification scheme for observed spatio-temporal patterns. We mention the important generalization of Kishimoto and Amari (30) in lateral-inhibition type fields in the absence of transmission delay. Since neurophysiological properties of observed neural tissue are not accessible precisely, a classification scheme might link model functionals with observed phenomena. For example, observed traveling waves necessitate a mean interaction time beyond a certain threshold defined by synaptic kernel properties. In addition, this classification might be important for estimating interaction parameters from multi-site neuronal data (58). Due to the large number of different activity phenomena, further studies in this area could incorporate additional mechanisms like standing and traveling pulse fronts (59) or the consideration of feedback delay (60; 61; 62).

References

- [1] M. Gazzaniga (Ed.), *The new cognitive neurosciences*, MIT Press, Cambridge, 2000.
- [2] J. Kelso, *Dynamic Patterns: The Self-Organization of Brain and Behavior*, MIT Press, Cambridge, 1995.
- [3] W. J. Freeman, *Neurodynamics: An Exploration in Mesoscopic Brain Dynamics*, Springer-Verlag, Berlin, 2000.
- [4] P. Tass, *Phase resetting in medicine and biology : stochastic modelling and data analysis*, Springer, Berlin, 1999.
- [5] F. H. L. da Silva, W. Blanes, S. Kalitzin, J. Parra, P. Suffczynski, D. Velis, Epilepsies as dynamical diseases of brain systems: basic models of the transition between normal and epileptic activity, *Epilepsia* 44 (Suppl. 12) (2003) 72–83.
- [6] J. R. Brasic, Hallucinations, *Percep. Motor Skills* 86 (1998) 851
- [7] S. H. Isaacson, J. Carr, A. J. Rowan, Ciprofloxacin-induced complex partial status epilepticus manifesting as an acute confusional state, *Neurol.* 43 (1993) 1619
- [8] G. B. Ermentrout, J. D. Cowan, A mathematical theory of visual hallucination patterns, *Biol. Cybern.* 34 (1979) 137
- [9] V. K. Jirsa, H. Haken, Field theory of electromagnetic brain activity, *Phys. Rev. Lett.* 7 (5) (1996) 960
- [10] C. Uhl (Ed.), *Analysis of Neurophysiological Brain Functioning*, Springer-Verlag, Berlin, 1999.
- [11] A. Hutt, H. Riedel, Analysis and modeling of quasi-stationary multivariate time series and their application to middle latency auditory evoked potentials, *Physica D* 177 (2003) 203
- [12] H. Haken, *Principles of Brain Functioning*, Springer, Berlin, 1996.
- [13] W. J. Freeman, A model for mutual excitation in a neuron population in olfactory bulb, *IEEE Trans. Biomed. Engin.* 21 (1974) 350
- [14] J. C. Mosher, P. S. Lewis, R. M. Leahy, Multiple dipole modeling and localization from spatio-temporal meg-data, *IEEE Trans. Biomed. Eng.* 39 (6) (1992) 541
- [15] P. A. Robinson, P. N. Loxley, S. C. O'Connor, C. J. Rennie, Modal analysis of corticothalamic dynamics, electroencephalographic spectra and evoked potentials, *Phys. Rev. E* 63 (2001) 041909.

- [16] W. Gerstner, Time structure of the activity in neural network models, *Phys. Rev. E* 51 (1) (1995) 738
- [17] P. Bressloff, S. Coombes, Physics of the extended neuron, *Int. J. Mod. Phys. B* 11 (20) (1997) 2343
- [18] B. Ermentrout, Neural networks as spatio-temporal pattern-forming systems, *Rep. Prog. Phys.* 61 (1998) 353
- [19] W. M. Kistler, R. Seitz, J. L. van Hemmen, Modeling collective excitations in cortical tissue, *Physica D* 114 (1998) 273
- [20] R. Ben-Yishai, R. L. Bar-Or, H. Sompolinsky, Theory of orientation tuning in visual cortex, *Proc. Natl. Acad. Sci.* 92 (1995) 3844
- [21] T. Wennekers, Dynamic approximation of spatio-temporal receptive fields in nonlinear neural field models, *Neural Comp.* 14 (2002) 1801
- [22] K. J. Friston, Transients, metastability and neuronal dynamics, *NeuroImage* 5 (1997) 164
- [23] J. Eggert, J. L. van Hemmen, Unifying framework for neuronal dynamics, *Phys. Rev. E* 61 (2) (2000) 1855
- [24] H. R. Wilson, J. D. Cowan, Excitatory and inhibitory interactions in localized populations of model neurons, *Biophys. J.* 12 (1972) 1
- [25] P. L. Nunez, *Neocortical dynamics and human EEG rhythms*, Oxford University Press, New York - Oxford, 1995.
- [26] A. Hutt, M. Bestehorn, T. Wennekers, Pattern formation in intracortical neuronal fields, *Network: Comput. Neural Syst.* 14 (2003) 351
- [27] F. M. Atay, A. Hutt, Stability and bifurcations in neural fields with finite propagation speed and general connectivity, *SIAM J. Appl. Math.* in press.
- [28] G. B. Ermentrout, J. D. Cowan, Large scale spatially organized activity in neural nets, *SIAM J. Applied Math.* 38 (1) (1980) 1
- [29] S. Amari, Dynamics of pattern formation in lateral-inhibition type neural fields, *Biol. Cybernetics* 27 (1977) 77
- [30] K. Kishimoto, S. Amari, Existence and stability of local excitations in homogeneous neural fields, *J. Math. Biology* 7 (1979) 303–318.
- [31] R. Osan, G. B. Ermentrout, The evolution of synaptically generated waves in one- and two-dimensional domains, *Physica D* 163 (2002) 217
- [32] S. M. Crook, G. B. Ermentrout, M. C. Vanier, J. M. Bower, The role of axonal delays in the synchronization of networks of coupled cortical oscillators, *J. Comput. Neurosci.* 4 (1997) 161

- [33] W. J. Freeman, Characteristics of the synchronization of brain activity imposed by finite conduction velocities of axons, *Int. J. Bif. Chaos* 10 (10) (2000) 2307
- [34] J. C. Eccles, M. Ito, J. Szentagothai, *The Cerebellum as a Neuronal Machine*, Springer-Verlag, New York, 1967.
- [35] W. J. Freeman, *Mass Action in the Nervous System*, Academic Press, New York, 1975.
- [36] J. Eggert, J. L. van Hemmen, Modeling neuronal assemblies: Theory and implementation, *Neural Comput.* 13 (9) (2001) 1923
- [37] V. B. Mountcastle, Modality and topographic properties of single neurons of cat's somatic sensory cortex., *Neurophysiol.* 20 (1957) 408
- [38] D. H. Hubel, T. N. Wiesel, Receptive fields of cells in striate cortex of very young, visually unexperienced kittens, *J. Physiol* 26 (1963) 994
- [39] K. J. Sanderson, The projection of the visual field to the lateral geniculate and medial interlaminar nuclei in the cat, *J. Comp. Neurol.* 143 (1971) 101
- [40] B. Katz (Ed.), *Nerve, Muscle and Synapse*, McGraw-Hill, New York, 1966.
- [41] W. J. Freeman, Tutorial on neurobiology: from single neurons to brain chaos, *Int. J. Bif. Chaos* 2 (3) (1992) 451
- [42] D. J. Amit, *Modeling brain function: The world of attractor neural networks*, Cambridge University Press, Cambridge, 1989.
- [43] J. Cowan, G. Ermentrout, Some aspects of the 'eigenbehavior' of neural nets, in: S. Levin (Ed.), *Studies in mathematical biology, part I: Cellular behavior and the development of pattern*, MAA, Washington DC, 1978, pp. 67
- [44] A. Turing, The chemical basis of morphogenesis, *Philos. Trans. R. Soc. London* 327B (1952) 37
- [45] V. Castets, E. Dulos, J. Boissonade, P. D. Kepper, Experimental-evidence of a sustained standing turing-type non-equilibrium chemical-pattern, *Phys. Rev. Lett.* 64 (1990) 2953
- [46] L. Perko, *Differential Equations and Dynamical Systems*, Springer, Berlin, 1998.
- [47] H. Haken, *Advanced Synergetics*, Springer, Berlin, 1983.
- [48] J. Swift, P. Hohenberg, Hydrodynamic fluctuations at the convective instability, *Phys. Rev. A* 15 (1977) 319.
- [49] M. C. Cross, P. C. Hohenberg, Pattern formation outside of equilibrium, *Rev. Mod. Phys.* 65 (3) (1993) 851

- [50] H. R. Wilson, J. D. Cowan, A mathematical theory of the functional dynamics of cortical and thalamic nervous tissue, *Kybernetik* 13 (1973) 55
- [51] J. Rinzel, D. Terman, X. J. Wang, B. Ermentrout, Propagating activity patterns in large-scale inhibitory neuronal networks, *Science* 279 (1998) 1351
- [52] G. Tamas, E. H. Buhl, P. Somogyi, Massive autaptic self-innervation of gabaergic neurons in cat visual cortex, *J. Neurosci.* 17 (16) (1997) 6352
- [53] P. Levy, Sur certains processus stochastique homogènes, *Comp. Math.* 7 (1939) 283
- [54] W. Feller, *An introduction to probability theory and its applications*, Wiley, New York, 1966.
- [55] V. Bringuier, F. Chavane, L. Glaeser, Y. Fregnac, Horizontal propagation of visual activity in the synaptic integration field of area 17 neurons, *Science* 283 (1999) 695
- [56] J. J. Wright, D. T. J. Liley, A millimetric-scale simulation of electrocortical wave dynamics based on anatomical estimates of cortical synaptic density, *Biosyst.* 63 (2001) 15
- [57] B. Gough, *GNU Scientific Library Reference Manual*, 2nd Edition, Network Theory Ltd, 2003.
- [58] O. François, C. Larota, J. Horikawa, T. Hervé, Diffusion and innovation rates for multidimensional neuronal data with large spatial covariances, *Network: Comput. Neural Syst.* 11 (2000) 211
- [59] D. J. Pinto, G. B. Ermentrout, Spatially structured activity in synaptically coupled neuronal networks: I. travelling fronts and pulses, *SIAM J. Applied Math.* 62 (1) (2001) 206
- [60] A. Engel, O. Koenig, A. Kreiter, W. Singer, Interhemispheric synchronization of oscillatory neuronal response in cat visual cortex, *Science* 252 (1991) 1177–1179.
- [61] M. Steriade, D. McCormick, T. Sejnowski, Thalamocortical oscillations in the sleeping and aroused brain, *Science* 262 (1993) 679–685.
- [62] A. Knoblauch, F. Sommer, Synaptic plasticity, conduction delays, and inter-areal phase relations of spike activity in a model of reciprocally connected areas, *Neurocomputing* 52-54 (2003) 301–306.
- [63] P. A. Robinson, C. J. Rennie, J. J. Wright, Propagation and stability of waves of electrical activity in the cerebral cortex, *Phys. Rev. E* 56 (1) (1997) 826

Figure 1: Illustration for the detection of constant stationary solutions of Eq. (8). For $I_0 < 1.32$, there are three solutions, while for $I_0 > 1.32$ there is only a single one at large values of V_0 . Simple iteration studies near the solutions reveal their stability: Filled circles represent stable fixed points, while empty circles illustrate unstable fixed points. At the critical value $I = 1.32$, there is a saddle node solution (hatched circle) synchronous to a stable fixed point at large values of V_0 , cf. Fig. 2. Here, we applied the sigmoid function $S = 1/(1 + \exp(-c(V - V_r)))$ (35; 63), $a_e = 10$, $a_i = 5$ and $c = 1.8$, $V_r = 3.0$ (56).

Figure 2: Bifurcation diagram and nonlinear gain for constant bifurcations for $a_e > a_i$. Left panel: Stability of the stationary state V_0 with respect to external input I_0 . For $a_e - a_i > 4/c = 2.22$, both stable (solid line) and unstable branches (dashed line) exist, while for $a_e - a_i \leq 2.22$ there is only a single stable solution. Right panel: The nonlinear gain s with respect to the constant state V_0 . The horizontal line $s = 1/(a_e - a_i)$ separates stable from unstable states and determines the critical values of V_0 . In both panels, we applied the sigmoid function introduced in Fig. 1.

Figure 3: Necessary parameter regime for nonstationary instabilities for diverse mean excitatory interaction time τ_e and synaptic delay constant γ . Valid parameters (hatched area) are constrained by the threshold of Eq. (18) plotted as solid line, the threshold of constant bifurcation (dotted line) and the threshold of asymptotic stability (dashed line).

Figure 4: Expansion factors β^2 and ϵ plotted with respect to the control parameter s . The solid line part gives the parameter range of stable solutions V_0 , for which Turing instabilities might occur. The dashed line part denotes the parameter domain of unstable stationary solutions V_0 , cf. Fig. 2. In both panels $a_e = 8$, $a_i = 5.0$, and we applied the sigmoid function introduced in Fig. 1.

Figure 5: The factor Π of the cubic term in Eq. (33) plotted with respect to the bifurcation threshold s_c from Eq. (15) for various ξ_e, ξ_i . Each suitable parameter set a_e, a_i, ξ_e, ξ_i maps to a maximum of $\hat{K}(k)$ and thus a single value s_c . Thus the plots have been computed by decreasing a_e leading to increasing s_c , while $0 < a_e - a_i < 4/c$. The range of a_e depends on ξ_e, ξ_i . The parameters have been chosen as $a_i = 5.0$, $\gamma = 2.1$ and the sigmoid function is as in Fig. 1.

Figure 6: Potential V_{pot} and bifurcation diagram of the order parameter equation (33). It has been found that $k_c = 0.6$, $s_c = 0.423$ and $V_0 = 2.723$ at s_c with parameters $a_e = 6.0$, $a_i = 5.0$, $\xi_e = 1.0$, $\xi_i = 2.0$, $\gamma = 2.1$ and the sigmoid function from Fig. 1.

Figure 7: Excitatory and inhibitory kernels for various parameters. All kernels are finite except for $K_e(x)$ for $p = 0.5$. In case of $\xi_e > 1$, the excitatory kernel $K_e(x)$ exhibits a maximum at $x = \xi_e - 1$. We point out that $\xi_e < 1$ yields divergent excitatory self-connectivity, while the excitatory self-connectivity vanishes for $\xi_i > 1$.

Figure 8: Sufficient parameter regimes of Turing patterns with respect to spatial interaction ranges ξ_i , ξ_e and various values of a_e/a_i . The thin solid line denotes $\xi_i = \xi_e$, while filled and empty squares, triangles and diamonds mark different cases discussed in Figs. 9 and 10.

Figure 9: Function $\hat{K}(k)$ for $\xi_e < \xi_i$. Parameter values are chosen according to Fig. 8. Both values of ξ_e allow a local maximum of $\hat{K}(k)$ for $k > 0$ and thus facilitate Turing patterns. Here, $a_e = 10$ and $a_i = 5$.

Figure 10: The kernel function $a_e K_e(x) - a_i K_i(x)$ and the function $\hat{K}(k)$ for $\xi_e \geq \xi_i$. Parameter values are chosen according to Fig. 8. In case of $\xi_e = 1.0$, local excitation-lateral inhibition ($\xi_i = 1.10$) yields a local maximum of \hat{K} , i.e. Turing patterns, while local inhibition-lateral excitation ($\xi_i = 0.90$) prohibits Turing patterns. In contrast, $\xi_e = 2.0$ exhibits local inhibition-lateral excitation for both values of ξ_i , while \hat{K} shows a local maximum for $\xi_i = 1.96$. Here, $a_e = 5$, $a_i = 5$.

Figure 11: Plots of the traveling wave speed v_{ph} with respect to the transmission speed v_e for various parameters ξ_e, ξ_i . For $\xi_e < 1$, the field reveals traveling waves for local excitation and lateral inhibition, which strongly contrasts to previous findings. The plots show an increase of v_{ph} by decreasing the inhibitory range ξ_i and increasing the excitatory range ξ_e . The applied parameters are $a_e = 60, a_i = 55, v_i = 100$ and $\gamma = 2.1$.

Figure 12: Space-time plot revealing the Turing instability for local excitation-lateral inhibition interaction. Parameters are set to $\xi_e = 1.0, \xi_i = 2.0, a_e = 6.0, a_i = 5.0$ with external stimulus $I_0 = 2.36$ yielding $V_0 = 2.75$ and $s_c = 0.428, k_c = 0.589$. The temporal evolution is calculated with $dt = 0.01$ while the space is discretized with $dx = 0.08, N = 400$. The greyscale encodes the deviation from the stationary state. The resulting pattern wavenumber agrees well with k_c .

Figure 13: Space-time plot revealing the Turing instability for local inhibition-lateral excitation interaction. Parameters are set to $\xi_e = 2.0, \xi_i = 1.92, a_e = 131.0, a_i = 130.0$ with external stimulus $I_0 = 2.2$ yielding $V_0 = 2.48$ and $s_c = 0.365, k_c = 0.24$. The temporal evolution is calculated with $dt = 0.01$ while the space is discretized with $dx = 0.15, N = 400$. The greyscale encodes the deviation from the stationary state. The resulting pattern wavenumber agrees well with k_c .

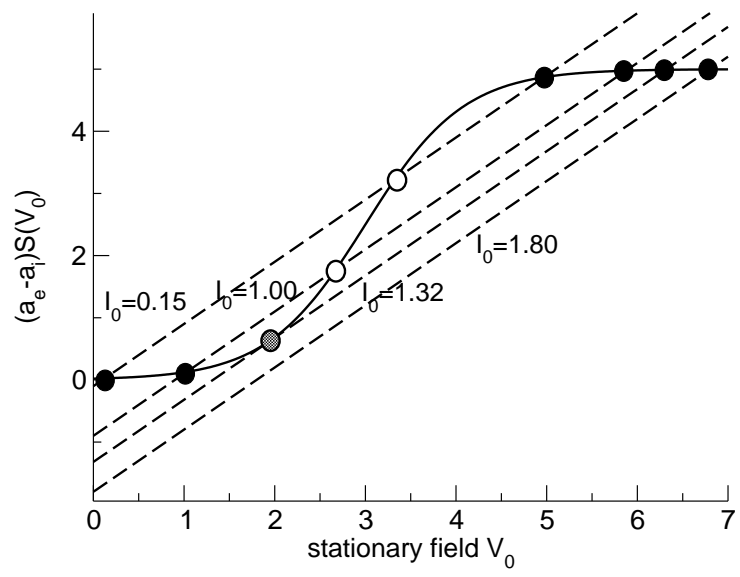


Figure 1

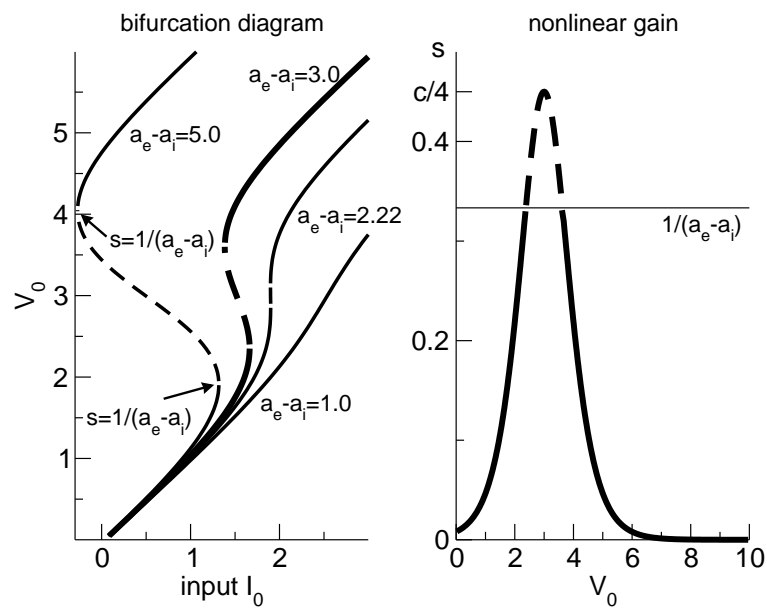


Figure 2

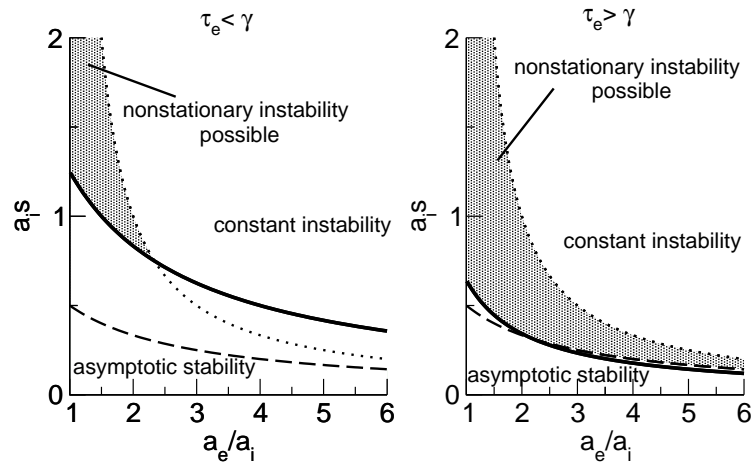


Figure 3

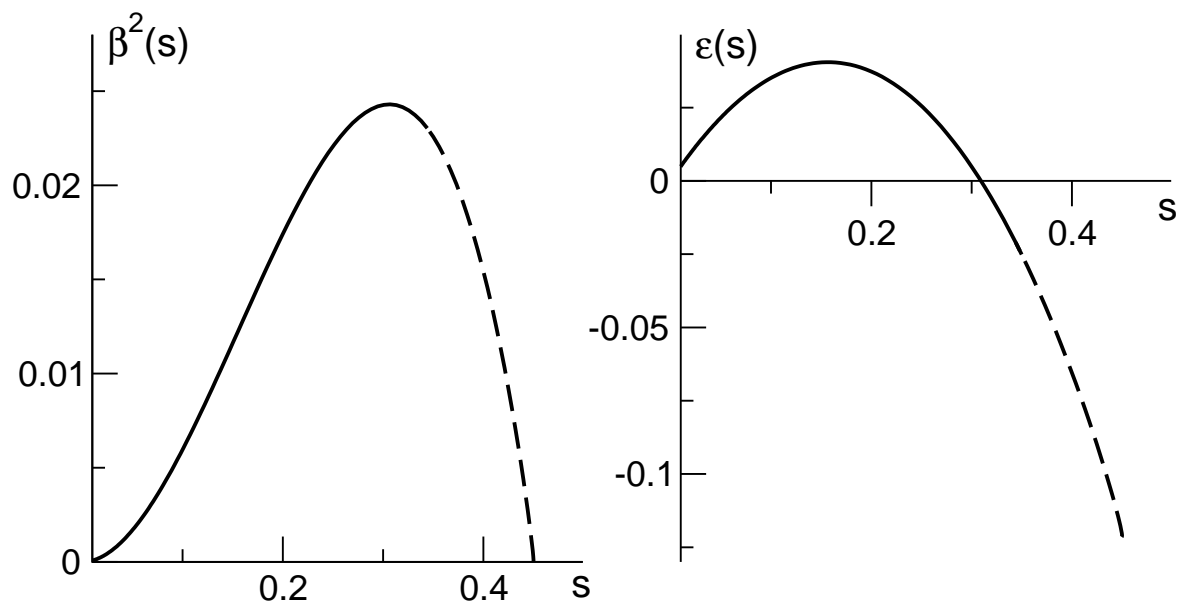


Figure 4

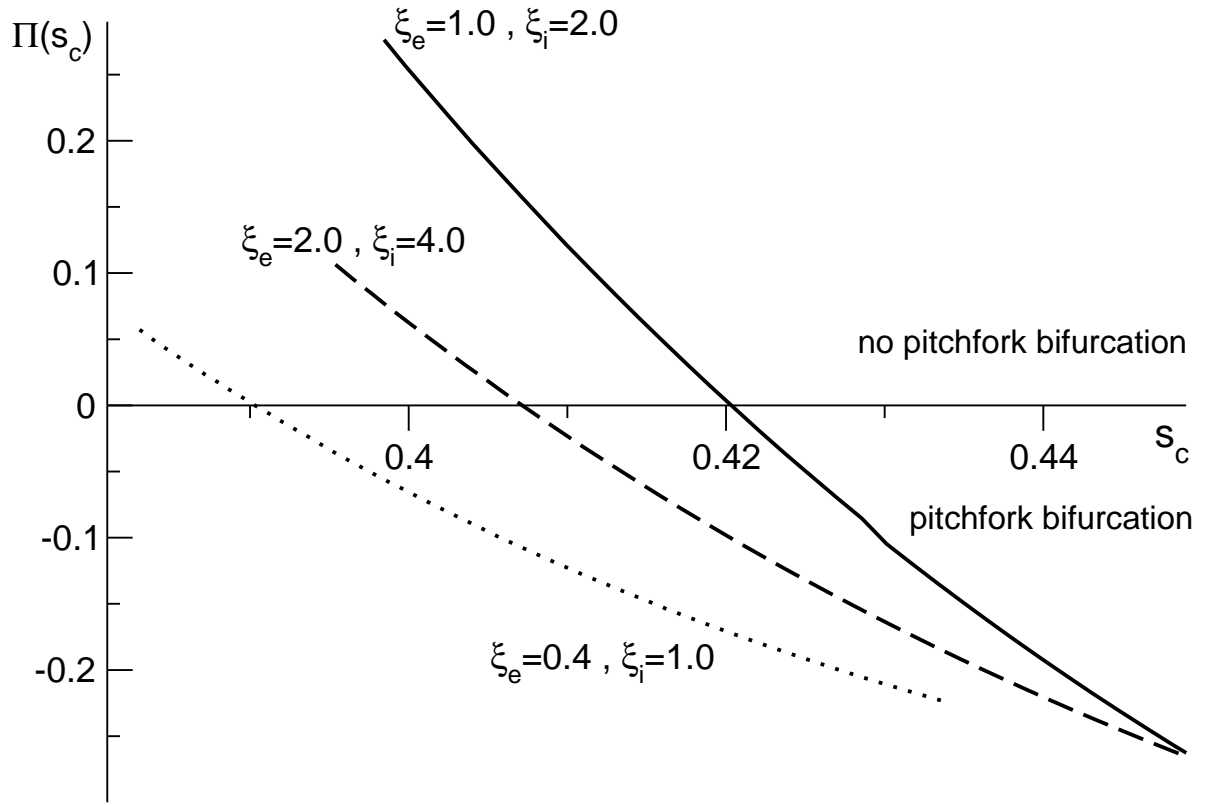


Figure 5

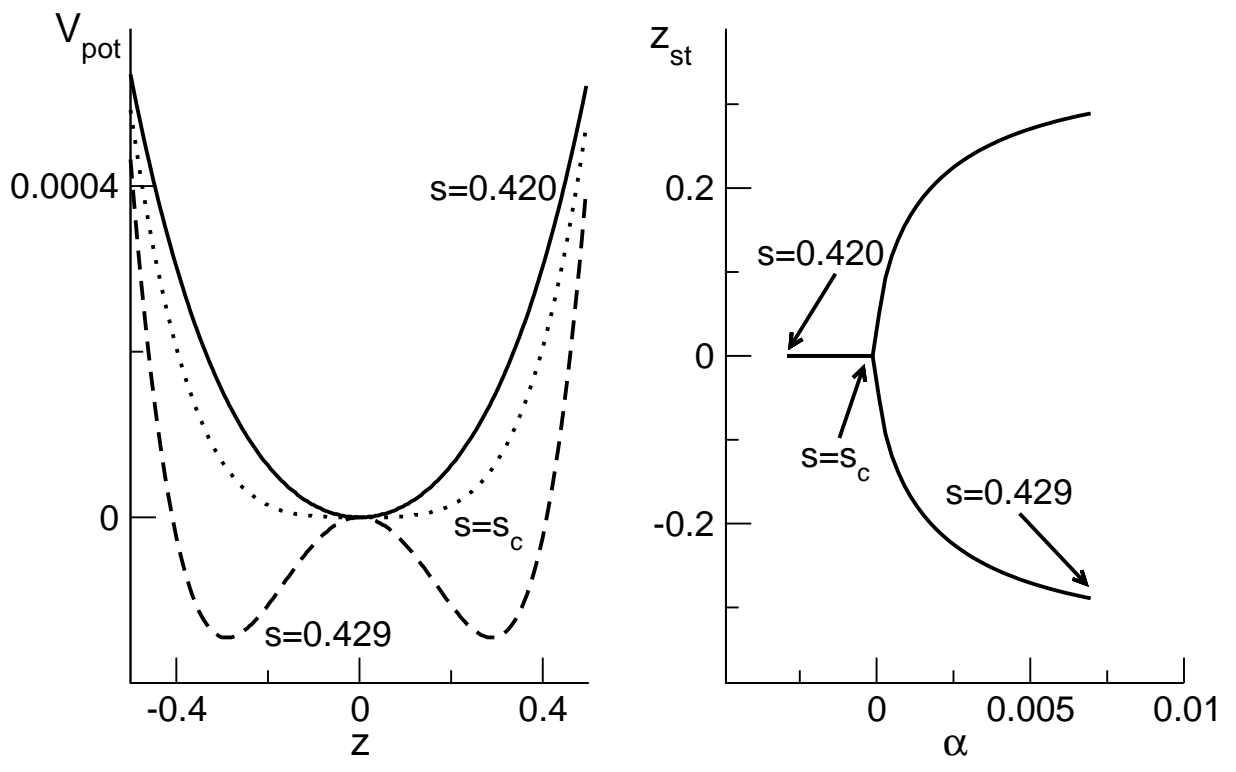


Figure 6

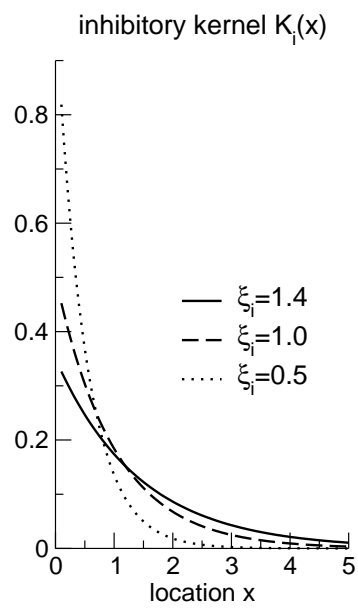
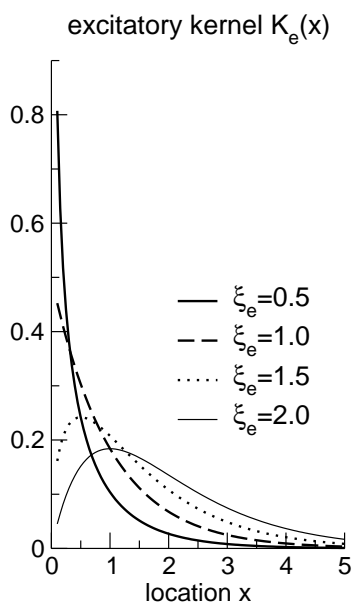


Figure 7

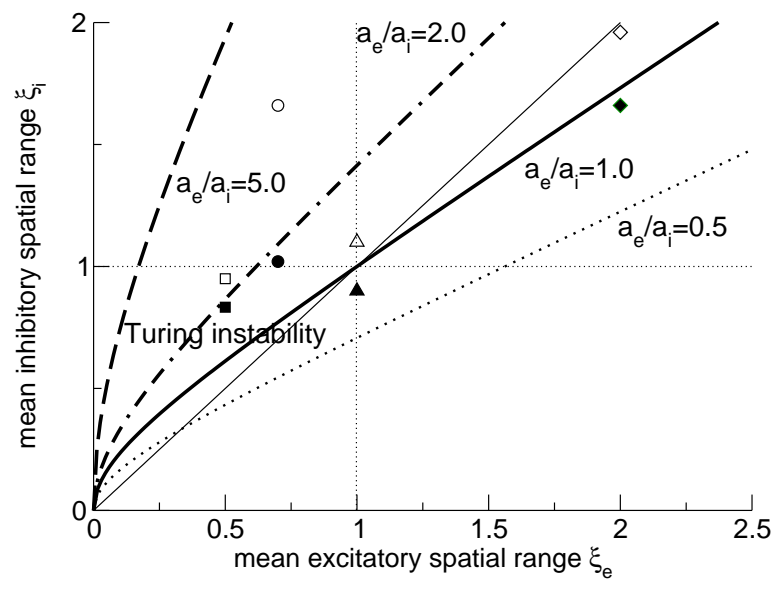


Figure 8

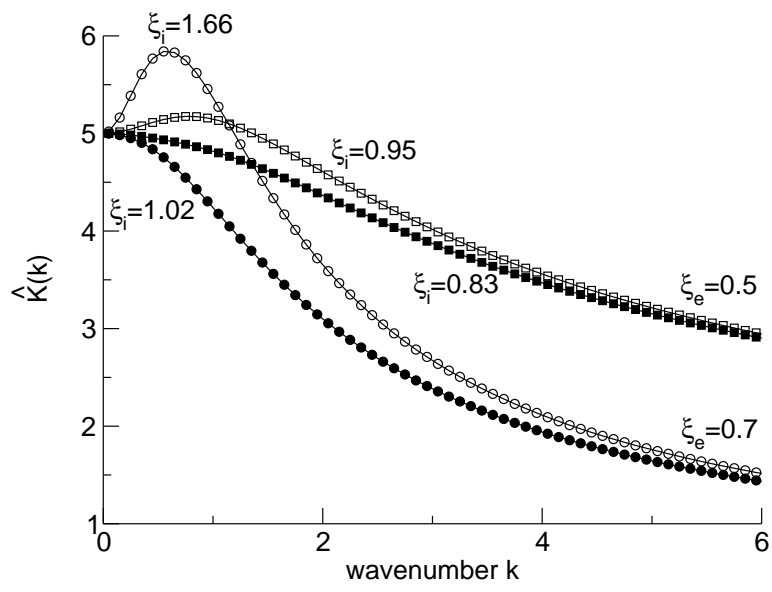


Figure 9

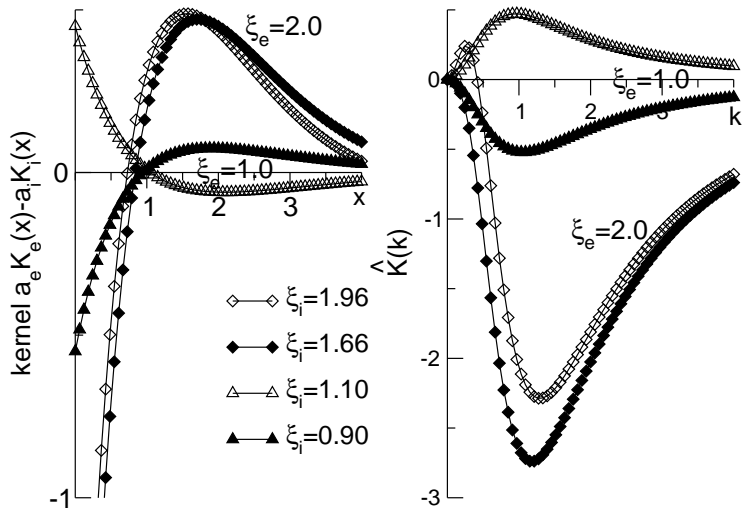


Figure 10

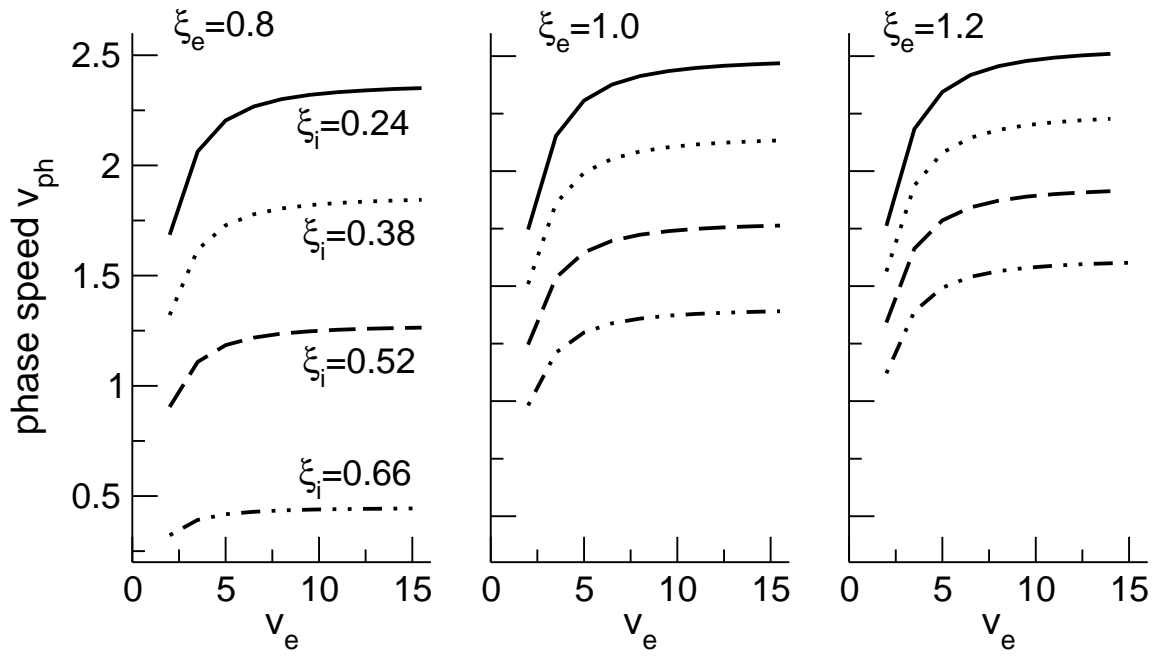


Figure 11

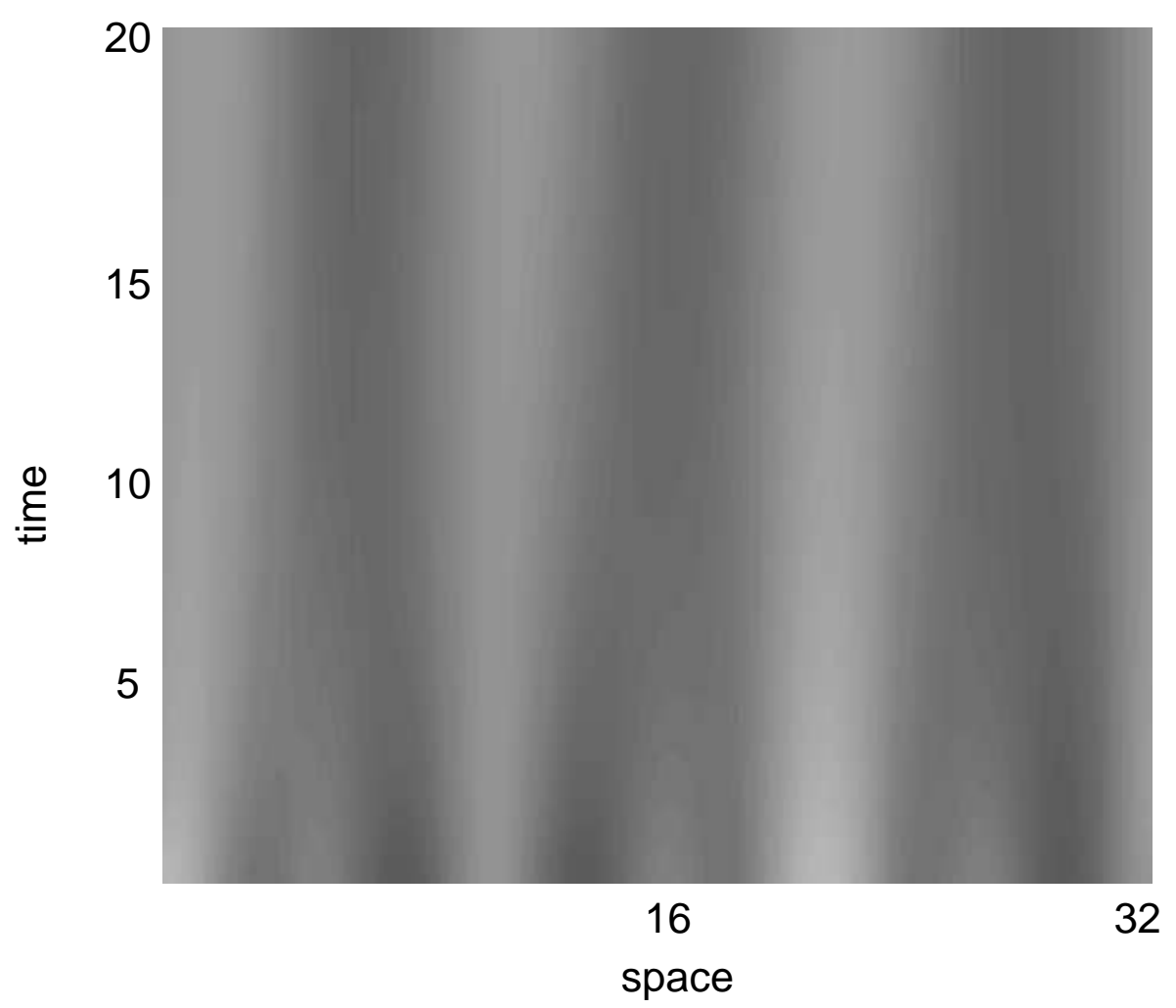


Figure 12

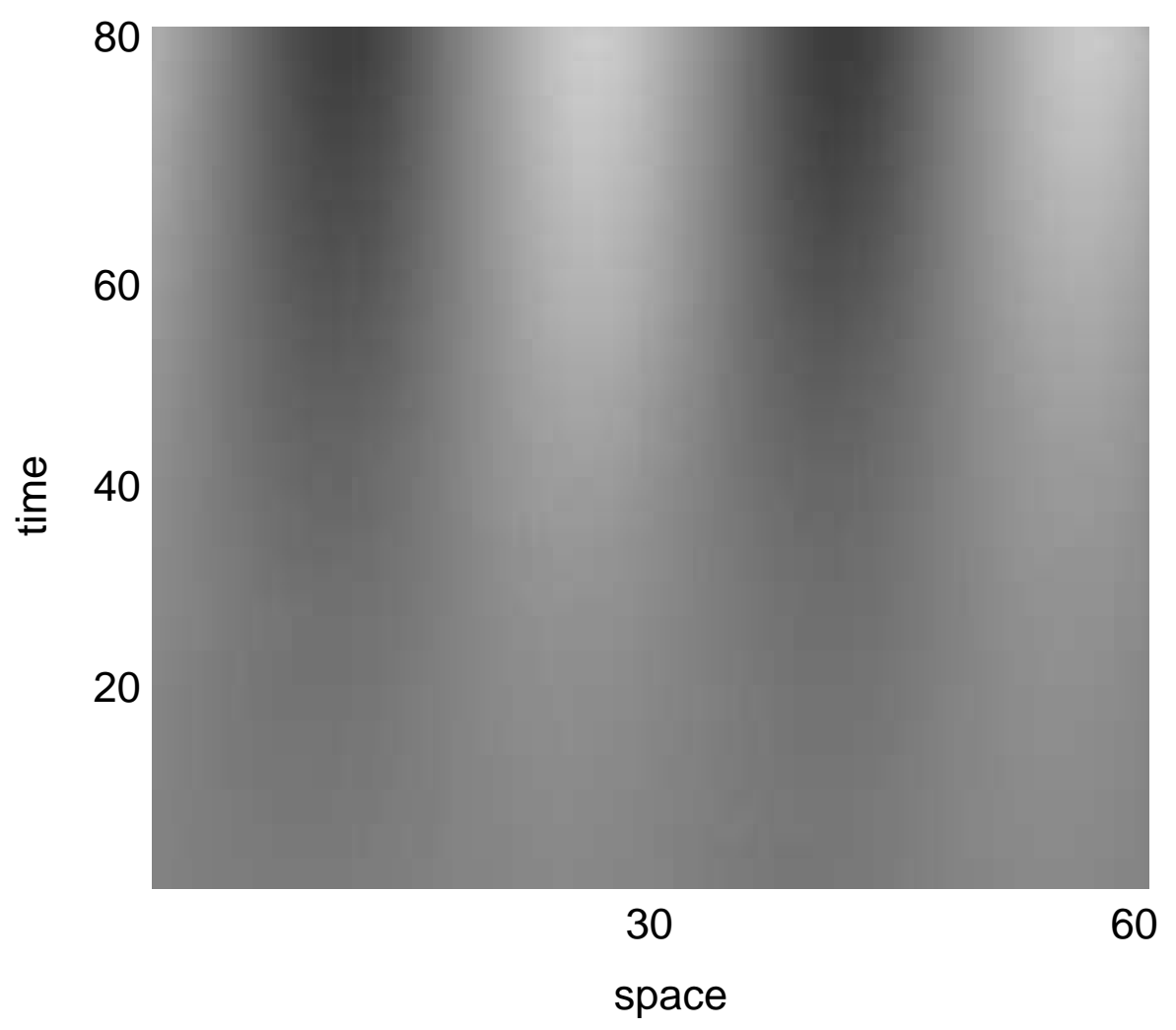


Figure 13